Single-atom dispersed Zn-N_3 active sites bridging the interlayer of g-C_3N_4 to tune NO oxidation pathway for the inhibition of toxic by-product generation

Ruiyang Zhang[a,b], Yuehan Cao[b], Dmitry E. Doronkin[d], Minzhi Ma[b], Fan Dong[c], Ying Zhou[a,b,*]

[a] State Key Laboratory of Oil and Gas Reservoir Geology and Exploitation, Southwest Petroleum University, Chengdu 610500, China

[b] Institute of Carbon Neutrality & School of New Energy and Materials, Southwest Petroleum University, Chengdu 610500, China

[c] Research Center for Environmental and Energy Catalysis, Institute of Fundamental and Frontier Sciences, University of Electronic Science and Technology of China, Chengdu 611731, China

[d] Institute of Catalysis Research and Technology and Institute for Chemical Technology and Polymer Chemistry, Karlsruhe Institute of Technology, Karlsruhe 76131, Germany

[*] E-mail address: yzhou@swpu.edu.cn (Y. Zhou).

Keywords: Single atom catalyst, Zn-N_3 active sites, Photocatalysis, Environmental remediation, Secondary pollution control

Abstract: Photocatalysis is regarded as one of the most promising methods for removing low concentrations of nitrogen oxides (NOx) discharged from mobile sources, but its low activity and secondary contamination with harmful by-products restrict its practical implementation. Herein, we introduced single Zn atoms into the interlayer of g- C_3N_4 prepared through a simple pyrolysis method with an ultrahigh loading amount of 37.0 wt% (10.2 at%). Zn-N_3 bridging structure is created by single atomic scattered Zn atoms connecting with three N atoms of two layers of g-C_3N_4, which enhance visible light absorption and electron-hole pairs' separation. The introduced single Zn atom induced the adsorbed O_2 and NO to fabricate the Zn-O_2-NO structure, which facilitated the dissociation of O_2 and the direct formation of nitrate from NO, tuning NO oxidation pathway and resulting in increased NO oxidization (49 %) but low toxic NO_2 generation (2.6 %). This current work introduces a novel approach to fabricating single-atom catalysts for highly effective environmental remediation and secondary pollution control.

1. Introduction

Nitrogen oxides (NOx) have been endangering the natural environment and human health around the world [1,2]. In general, NOx emissions are mostly created by the combustion of fossil fuels and include emissions from both stationary (industrial exhaust) and mobile (automobile exhaust) sources [3,4]. As automobile ownership grows, the problem of mobile

source NOx treatment becomes more pressing. Although most NOx in the automotive exhaust may be eliminated by the exhaust gas treatment system, the buildup of low-concentration NOx in the surrounding environment will result in a continual increase in NOx concentration, posing a major health risk to people. As a result, dealing with a low concentration of NOx has become a serious challenge. Photocatalysis, which converts solar energy to chemical energy to purify pollutants, is one of the best solutions for treating low concentration NOx [5,6]. Photocatalysts can be used as a coating on acoustic insulation boards to treat low-concentrations NOx from mobile sources under solar light illumination and reduce their impact on the environment [7,8]. However, the photocatalytic activity is limited because of the poor migration driving strength of low concentration NOx. Furthermore, the NO_2 produced as a byproduct of NO oxidation is readily polluted [9,10]. As a result, one of the current research goals is the creation of efficient catalysts as well as the avoidance of subsequent contamination by hazardous by-products. For a decade, single-atom catalysts have sparked great interest for environmental remediation originated from the high atom efficiency and product regulation ability, which have been dubbed the bridge between homogeneous and heterogeneous catalysis [11–14]. Therefore, through structural design, single-atom catalysts may be anticipated to effectively suppress hazardous byproducts while simultaneously meeting the activity requirements of treating low concentration of NOx [15–18]. However, since the single atom is in a semi-stable state, it may aggregate into clusters or particles, reducing the catalytic activity [19,20]. Therefore, improving the interaction between the single atom and the substrate, as well as increasing the loading amount, remain major problems in the development of single-atom catalysts. Previous research has shown that the d orbital of transition metals can form strong bonds with the N 2p orbital [21,22]. Thus, as an *N*-rich catalyst, graphitic carbon nitride (g-C_3N_4) shows significant promise for the support of single transition metal atoms [23–25]. Due to the abundance of N atoms, g-C_3N_4 has a lot of natural defects with exposed nitrogen edges to preserve minimum energy, which are good anchor locations for single transition metal atoms [26,27]. Additionally, previous studies showed that the powerful interaction between single Mo atoms and g- C_3N_4 might cause a significant change in the g-C_3N_4 structure including amorphous transformation, significantly extending the visible light sensitivity [28]. Moreover, researchers have also demonstrated that formatting an efficient charge carrier channel between the interlayers of g-C_3N_4 could speed up the separation of generated charge carriers [29]. As a result, it is possible that linking single transition atoms with the N atoms of two layers of g-C_3N_4 could extend visible-light response while simultaneously promoting charge carrier separation, leading to extremely photocatalytic performance. Based on the foregoing, Zn-doped g-C_3N_4 (Zn-CN) was fabricated using a pyrolysis process. Theoretical calculation and XAFS confirmed single Zn atom bridged the interlayer of g-C_3N_4 through the fabrication of the Zn-N_3 coordination structure. The powerful interaction between single Zn atoms caused the g-C_3N_4 structure to be destroyed, reinforcing visible light response, while the intercalated single Zn atom between the layers of g-C_3N_4 sped up the transfer of charge carriers. More importantly, the creation of Zn-O_2-NO from adsorbed O_2 and NO promoted NO direct oxidization to nitrate with a low energy barrier, preventing the production of the hazardous NO_2 byproduct that often results from g-C_3N_4-based catalysts [30–32]. Our work provides fresh insight into the fabrication of single-atom catalysts for enhancing photocatalytic activity and hindering toxic by-product pollution.

2. Experiments

2.1. Materials

In this work, we employed analytical pure reagents for the experiments which were all purchased from Chengdu Kelong Chemical Co., ltd. Deionized water was employed as the solution.

2.2. The fabrication of samples

In a typical preparation process, 15 g urea was dissolved in 200 mL deionized water and then different amounts of zinc acetate were added to the above solution. After stirring for 30 min, the solution was frozen-drying for 24 h to remove the water and heated at 550 ◦C for 1 h in a crucible with a cover to achieve Zn-CN. Based on the atomic amount of zinc atoms, the obtained samples were named as g-C_3N_4 (0 %), Zn-CN- 0.05 (0.05 %), Zn-CN-0.25 (0.25 %), Zn-CN-0.5 (0.5 %), Zn-CN-0.75 (0.75 %), Zn-CN-1 (1 %) and Zn-CN-2 (2 %). For comparison, different metals (Ti, V, Cr, Mn, Fe, Co, Ni, and Cu) doped g-C_3N_4 were prepared through a similar method using different precursors (butyl titanate, ammonium metavanadate, chromic acetate, manganese acetate, ferric acetate, acetylacetone cobalt, nickel acetate, and cupric acetate).

2.3. Characterization

Powder X-ray diffraction (XRD, PANalytical X'pert diffractometer) of samples measured at 40 kV and 40 mA using Cu Kα radiation was performed to study the crystal structure. The morphology and microstructure of samples were investigated through a scanning electron microscope (SEM, ZEISS EVO MA15 microscope) and transmission electron microscope (TEM, FEI Tecnai G220 microscope). The single Zn atom was confirmed through aberration-corrected high-angle annular dark-field scanning transmission electron microscopy (HAADF-STEM) conducted on a JEOL ARM200CF with a dual-type EDS detector (JED- 2300 T). The surface functional groups and states of samples were researched by Fourier transform infrared (FTIR) and X-ray photoelectron spectroscopy (XPS) on a Thermo Nicolet 6700 spectrometer and Thermo Scientific Escalab 250Xi spectrometer, respectively. UV–vis diffuse reflectance spectroscopy (UV–vis DRS), photoluminescence (PL), and time-resolved PL spectra were performed on Shimadzu UV-2600 spectrophotometer, Hitachi F-7000 fluorescence spectrometer, and HORIBA FM4-2015 spectrometer. The surface area and pore structure were investigated through N2 adsorption and desorption isotherm on Micromeritics ASAP 2020 Plus automated gas sorption techniques. Electron spin resonance (ESR) spectroscopy was carried out on a JES-FA200 spectrometer at room temperature using 5, 5-dimethyl-1-pyrroline *N*-oxide (DMPO) as the trapping agent. Moreover, the superoxide radical (•O2) and hydroxyl radical (•OH) were recorded by applying methyl alcohol and water as the solvent under light illumination (300 W Xenon lamp).

2.4. Catalytic test

Photocatalytic NO oxidation of samples was tested under visible-light illumination. The reaction was performed in a homemade reactor and the samples were prepared as follows: Firstly, double 100 mg samples were put into 20 mL of deionized water and placed into two glass culture dishes (12 cm). Then, the above-prepared dishes were heated at 80 ◦C to remove water. Finally, the dried dishes were put into the reactor. A 150 W metal halide lamp (λ greater than 420 nm) was used as a light source and placed on the reactor. The initial concentration of NO is 600 ppb through the control of the flow rates of air (2 L/ min) and NO gas cylinders (100 ppm using N_2 as balance gas, 11 mL/ min). NO and NO2 concentrations were measured using NOx analyzer (Thermo Scientific, 42i-TL).

2.5. Theoretical calculation method

The Cambridge Sequential Total Energy Package (CASTEP) code with the Generalized Gradient Approximation (GGA) of the Perdew- Burke-Ernzerhof (PBE) method in Materials Studio Software was utilized in our calculations [33–35]. The Monkhorst-Pack k-point was 2 × 2 × 1, while the cut-off energy and configuration of the maximum energy change were 380 eV and 2×10^{-5} eV/atom. For the investigation of introduced points and the transition states (TS), g-C_3N_4 with a 1 × 2 × 4 supercell was cleaved along with the (0 0 1) orientation. The formation energy after the introduction of the Zn atom was calculated through the following equation:

$$E_{\text{Formation energy}} = E(\text{g-}C_3N_4 + \text{Zn atom}) - E(\text{g-}C_3N_4) - E(\text{Zn atom}) \quad (1)$$

where E(g-C_3N_4 + Zn atom) is the total energy of Zn doped g-C_3N_4 through intercalation, load, or replacement; E(g-C_3N_4) and E(Zn atom) are the energy of g-C_3N_4 and Zn atom, respectively.

2.6. In situ DRIFTS

In situ DRIFTS was measured on a Bruker TENSOR II FTIR spectrometer with an in situ diffuse reflectance cell (Harrick) and a point light source (Model MVL-210, Japan). A typical test process is as follows: Firstly, the sample was pretreated at 100 °C under He flow to clear the surface. Then, the sample was put into the Harrick cell and the background was recorded. Next, the sample was flowed by NO (50 ppm, 50 mL/min) and pure O_2 (50 mL/min) to achieve adsorption–desorption equilibrium. Finally, the data was measured under dark and light illumination.

3. Results and Discussions

3.1. Structure and morphology

The structure of Zn-CN was first investigated through the XRD patterns. XRD diffraction peaks at 13.0 and 27.5◦ of g-C_3N_4 were corresponding to the (1 0 0) and (0 0 2) planes (Fig. 1a) [36,37]. The strength of these two peaks reduced after Zn atoms were introduced, and they vanished when the quantity of Zn was more than 0.5 %, revealing the broken long-range order of g-C_3N_4 originated from the interaction between g-C_3N_4 and Zn atoms. A broad diffraction peak in the range of 15–25◦ was found, which might be due to the increased interlayer distance of g-C_3N_4 through the insertion of Zn atoms into its interlayer. FTIR spectra of various Zn-CN ratios are displayed in Fig. 1b. Three primary bands at 810, 3201, and 3419 cm^{-1} of g-C_3N_4 are assigned to triazine unit, –NH, and –OH bonds, respectively, whereas the bands at 1150–1650 cm^{-1} are attributed to C–N heterocycles [38,39]. The band of the triazine unit changes to 806 cm^{-1} when Zn atoms are introduced, showing the powerful interaction between Zn atoms and g-C_3N_4. Moreover, even though the strength of these bands reduces with the addition of Zn atoms, all of the bands persist, suggesting that g-C_3N_4 maintains its short-range order. These findings support the altered structure of g-C_3N_4 after the addition of Zn atoms, which will affect photocatalytic activity.

The morphology and microstructure before and after the addition of Zn atoms were researched by TEM (Fig. 2a–d). The creation of gas during the pyrolysis process as the pore template results in an abundant porous structure in pure g-C_3N_4, however, this pore structure becomes irregular with the addition of zinc acetate precursor. Importantly, neither g-C_3N_4 nor Zn-CN showed any lattice fringes, indicating that the introduced Zn atoms have not agglomerated to

form a zinc compound. As demonstrated in Fig. 2e, aberration-corrected high-angle annular dark-field scanning transmission electron microscopy (HAADF-STEM) of Zn-CN was used to further verify the status of Zn atoms. The brilliant spots can be attributed to single Zn atoms, which is corroborated by the EDS element mapping (Fig. 2f). These results validate the single atomic dispersed Zn atoms, revealing that single Zn atoms doped g-C_3N_4 were effectively generated.

To verify the surface chemical groups and states of Zn-CN, XPS of different ratios of Zn-CN compared with pure g-C_3N_4 were carried out (Fig. 3). The binding energy of the C 1s peak was corrected at 284.8 eV. Except for the peak at 284.8 eV ascribed to the C–C bond, the high-resolution C 1s of g-C_3N_4 have two main peaks with binding energies of 286.5 and 288.0 eV, which are ascribed to C–O and N-C=N bonds [40,41], while the binding energies of these two peaks show significant shift for Zn-CN-0.5 (287.4 and 288.1 eV) and Zn-CN (286.2 and 288.1 eV). Furthermore, compared with g-C_3N_4 (398.5 and 399.5 eV), the binding energy of N 1s peaks assigned to C-N=C and N-$(C)_3$ bonds is considerably different for Zn-CN-0.5 (398.6 and 400.4 eV) and Zn-CN-2 (398.8 and 399.7 eV) [42,43]. The N 1s peak of g-C_3N_4 at 400.8 eV, which corresponds to the C–N–H bond [44], vanishes once Zn atoms are introduced, which might result from broken hydrogen bonds between the triazine units of g-C_3N_4, demonstrating the decrease of crystallinity. In the high-resolution O 1s spectrum, all of the samples have two peaks attributed to C–O–H and C–O–C bonds, with binding energies of 532.1 and 533.6 eV for pure g-C_3N_4 [45,46], 531.4 and 533.0 eV for Zn-CN-0.5, and 531.7 and 533.3 eV for Zn-CN-2, which could be due to the changed oxidized states caused by the increased amount of zinc acetate precursor. In addition, Zn-CN-0.5 has a Zn 2p peak with the binding energy of 1021.8 eV indicating the valence state of the Zn atom is +2 [47], which increases to 1022.1 eV for Zn-CN-2, demonstrating the increased oxidation state of Zn atoms. The aforementioned findings show a significant impact of Zn injection on the structure of g-C_3N_4, which is compatible with the outcomes of the theoretical calculations as follows.

3.2. Zn-CN structure

To investigate the introduced point of single Zn atoms, DFT calculation was employed. We have tried all the possible points that the Zn atom may introduce, and their optimized structures and corresponding formation energy are summarized (Fig. S1-3 and Table S1). Intercalation between the interlayers of g-C_3N_4 (Fig. S1), load on the g-C_3N_4 surface (Fig. S2), and replacement of the atoms of g-C_3N_4 (Fig. S3) are the three types of inserted Zn atoms. The formation energy of replacement is positive when compared to intercalation or load, indicating that it takes a lot more energy to replace the atoms of g-C_3N_4 with the inserted Zn atom. Even though the intercalation and load formation energies are relatively close, the average distance between the Zn atom and g-C_3N_4 for the load is too great, resulting in a weak interaction that contradicts the preceding analysis. After analyzing the several introduced locations of intercalation, the structure in which the Zn atom joins two layers of g-C_3N_4 has the lowest formation energy, indicating that it is the most probable Zn-CN structure. Further investigation reveals that the Zn atom forms Zn-N_3 active sites with three N atoms in this configuration, with a bond length of roughly 2.07 Å (Fig. 4a).

X-ray absorption fine structure (XAFS) of Zn-CN was compared with several reference samples to further confirm the Zn-CN structure. The XANES spectrum of Zn-CN differs from that of ZnO and zinc phthalocyanine, yet its edge position is identical to that of ZnO, implying that the oxidation state of Zn is +2, as determined by XPS analysis (Fig. 4b). Importantly, when

compared to ZnO, the edge position of Zn-CN is somewhat lower in energy, which is consistent with N atoms being the nearest neighbor atoms of Zn atoms due to N atom's lower electronegativity compared to O atom. When Zn-CN-0.5 and Zn-CN-2 samples are compared, the electronic structure differs somewhat. The first peak above the edge of the Zn-CN-2 sample is greater than the Zn-CN-0.5 sample, indicating that the coordination structures are different. The extended X-ray absorption fine structure (EXAFS) spectra of Zn-CN are shown in Fig. 4c in comparison to several reference samples. The EXAFS spectra of Zn-CN indicate largely just the first shell, which is made of light atoms (such as C, N, and O), with the primary peak at above the edge of the Zn-CN-2 sample is greater than the Zn-CN-0.5 sample, indicating that the coordination structures are different. The extended X-ray absorption fine structure (EXAFS) spectra of Zn-CN are shown in Fig. 4c in comparison to several reference samples. The EXAFS spectra of Zn-CN indicate largely just the first shell, which is made of light atoms (such as C, N, and O), with the primary peak at fitted R-factor is low (2 %), proving that the experiment and theoretic calculation are in good agreement. It's worth noting that the high-resolution XPS N 1s peak shows no Zn-N bond, which is due to the N- $(C)_3$ bond of g-C_3N_4 having comparable binding energy, as previously observed [48–50]. Moreover, the wavelet transform (WT) contour plots of Zn-CN differ greatly from ZnO (Zn-O bond) and Zn foil (Zn-Zn bond), but are similar to Zn phthalocyanine (Zn-N_4), confirming the Zn-N_3 bond structure (Fig. 4e–h). These findings support the almost similar structure derived from tests and theoretical calculations, indicating that the injected Zn atoms intercalate the g-C_3N_4 interlayer to produce Zn-N_3 active sites. It's important to note that Zn-CN-2 attained the maximum loading amount of single Zn atoms, which is 37.0 wt% (10.2 at%), surpassing the majority of single-atom catalysts previously reported [51–53].

3.3. Photocatalytic activity

The photooxidation of low-concentration NO under visible-light illumination was used to test the catalytic activity of Zn-CN. All samples were supplied with NO gas before illumination to achieve adsorption–desorption equilibrium. The photocatalytic NO elimination of several 3d transition metals doped g-C_3N_4 is demonstrated in Fig. S4. g-C_3N_4 shows NO removal ratio of 21 % after 30 min of visible light illumination, but after the addition of Ti, V, Cr, Mn, Fe, Co, Ni, Cu, and Zn atoms, it changes to 28 %, 0.1 %, 13 %, 12 %, 13 %, 21 %, 28 %, 0 %, and 32 %, respectively. The NO removal ratio of Zn doped g-C_3N_4 is the greatest which may be owing to its abundant active sites (Fig. S5), hence it was chosen for further study. The NO removal ratio of various quantities of Zn-CN is shown in Fig. 5a. The photocatalytic NO removal ratio increases initially, then drops, as the quantity of Zn increases. And Zn- CN-0.5 has the greatest NO elimination ratio of 49 %, and is greater than bulk Zn doped g-C_3N_4 (bulk Zn-CN) (Fig.S6), demonstrating the advantages of single-atom catalyst for photocatalytic NO oxidation. The NO removal ratio is lower than pure g-C_3N_4 when the Zn atoms amount is higher than 2 %, which might be due to the significantly disrupted g-C_3N_4 structure. The hazardous consequence of NO oxidation is NO_2, which can cause secondary pollution. The NO_2 production of several Zn- CN is shown in Fig. 5b. The NO_2 production fraction of pure g-C_3N_4 is 10 %, which decreases with the addition of Zn atoms. Zn-CN-0.5 has the lowest NO_2 production proportion (2.6 %), indicating that it is most oxidized. As a result, the Zn-CN-0.5 sample was chosen for the recycling experiment (Fig. 5c). After the first run, the NO removal ratio declines slightly before stabilizing at 42 % after four cycles, suggesting its good stability. Moreover, in situ DRIFTS of photocatalytic NO oxidation over the Zn-CN-0.5 sample were carried out as shown in Fig. 5d. As time went on, the bands at 1313, 1479, 1608 and 1631 cm^{-1} corresponding to monodentate

nitrate, ionic nitrate, and bridging nitrate increase and no other byproduct can be detected (Fig. S7), indicating that the main byproduct of NO oxidation is nitrate [54–56]. Moreover, Zn-CN shows considerable promise for environmental remediation because it is at the top of the research in terms of activity and harmful by-product hindering rates (Table S3) [30–32, 57–62]. These findings show that photocatalytic NO removal over Zn-CN-0.5 is effective while producing minimal levels of harmful NO_2.

3.4. Photocatalytic mechanism

The factors determining photocatalytic activity are frequently summarized as light absorption, carriers' separation, and surface reaction. Due to the limited fraction of high-energy UV light, a visible light response is required for light absorption as an effective photocatalyst [63]. DFT was used to determine the band structure and density of state (DOS) of g-C_3N_4 and Zn-CN (Fig. 6a). The bandgap of pure g-C_3N_4 is 2.7 eV, however, it drops to 2.15 eV when Zn atoms are added. The N 2p orbit dominates the top of the g-C_3N_4 valence band, whereas the C 2p orbit dominates the bottom of the conductive band. A new orbit assigned to the Zn 3d orbit can be seen in the deep valance band, which may be the explanation for the lowered bandgap. As a result, the diffuse reflection spectra of Zn-CN were measured. Pure g-C_3N_4 displays an absorption edge at around 412 nm (Fig. 6b), suggesting a bandgap of 3.01 eV, but the bandgap reduces with the addition of single Zn atoms to 2.98, 2.96, 2.94, 2.93, 2.96, 2.96, and 2.93 eV. Furthermore, in addition to the lowered bandgap, a new band tail arises in the 400–500 nm region, displaying increased light absorption. These findings show that Zn- CN can absorb a large range of visible light to generate more electron-hole pairs than pure g-C_3N_4.

To participate in the surface reaction, photogenerated charge carriers should migrate to the surface of a photocatalyst. Consequently, charge carriers' recombination reduces the ultimate photocatalytic activity. The photoluminescence (PL) spectra of several materials are shown in Fig. 6c. For the strong recombination of electron-holes pairs resulting from the quick transition on the plane of g-C_3N_4 and little migration between its interlayer, pure g-C_3N_4 has the maximum PL intensity. When single Zn atoms are introduced, the PL intensity diminishes dramatically as the number of Zn atoms increases. Three variables might be to blame for the decreasing PL intensity: (I) as a transition metal, the interaction between Zn atoms and g-C_3N_4 produces a Schottky barrier, which speeds up the passage of photogenerated electrons from g-C_3N_4 to Zn atoms; (II) as mentioned above, Zn atoms intercalate into the g-C_3N_4 interlayer and connect with two layers of g-C_3N_4 to form Zn-N_3 active sites, which promote charge carriers' transfer between the interlayer of g-C_3N_4; (III) single-atom dispersed Zn atoms have the highest atom efficiency to improve photogenerated electrons transfer. In addition, Fig. 6d depicts the time-resolved PL spectra of g-C_3N_4 and Zn-CN at various ratios. The lifespan of electrons created by pure g-C_3N_4 is 3.18 ns, which drops to 3.05 (0.5 %) and 3.02 (2 %), respectively, with the introduction of single Zn atoms, demonstrating the rapid electron transfer. These findings show that bridging Zn atoms can greatly reduce photogenerated charge carrier recombination, facilitating the transport of electrons and holes to the catalyst's surface.

To engage the photocatalytic redox, electron and hole will migrate to photocatalyst's surface. Pollutants adsorption is influenced by the surface area, which has an impact on the ultimate photocatalytic activity. As a result, in comparison to g-C_3N_4, the N_2 adsorption and desorption isotherms, as well as the BJH pore diameter distribution of Zn-CN, are presented in Fig. S8. The samples all show a Type IV isotherm and a distinct H3 hysteresis loop, confirming their mesoporous nature. Importantly, pure g-C_3N_4 has a surface area of 52.1 m^2/g, which rises

somewhat to 53.5 m^2/g for Zn-CN-0.5 and dramatically to 103.0 m^2/g for Zn-CN-2, whereas g-C_3N_4′ s pore volume (0.30 cc/g) reduces to 0.22 cc/g for Zn-CN-0.5 and subsequently increases to 0.43 cc/g for Zn-CN-2 (Table S4). These discrepancies in surface area and pore volume when compared to photocatalytic activity suggest that the number of active sites, rather than surface area, is one of the most important influencing variables. Single Zn atoms operate as active sites to boost photocatalytic activity, however, an excess number of added Zn atoms disrupts the structure of g-C_3N_4, reducing the active sites. Furthermore, the energy barriers of surface redox are influenced by the contact between the reactant and the catalyst, which has an impact on the ultimate catalytic activity. Thus, the transition states of NO oxidation over Zn-CN were estimated in comparison to pure g-C_3N_4, as shown in Fig. 7. In a typical NO oxidation process, NO combines with O_2 to produce NO_2, which is then further oxidized to produce nitrate. The energy battier for NO oxidation to NO_2 over g-C_3N_4 is 2.59 eV, whereas the energy battier for NO_2 further oxidation to nitrate is 2.89 eV. The weak interaction between the reactants (O_2 and NO) and g-C_3N_4 causes these large energy barriers. Whiles O_2 and NO combine to form the Zn-O_2-NO species when they are adsorbed on the Zn-CN surface. The increased band at 806 cm^{-1} as shown in DRIFTS is ascribed to the peroxide species, which confirms the formation of Zn-O_2-NO species [64–66]. This fantastic species could promote the O–O bond breakage (from 1.23 Å to 1.43 Å), improve reactive oxygen species generation as shown by the fact that Zn-CN exhibits stronger $\bullet O_2^-$ and •OH signals than pure g-C_3N_4 in ESR (Fig. S9), and convert NO to nitrate directly (1.36 eV), which avoids the generation of NO_2 and hinders the secondary pollution, demonstrating its great potential for air purification.

Therefore, the introduction of single Zn atoms enhanced visible light illumination, charge carriers transfer, and surface reaction while N atoms stabilized the Zn-N_3 structure to maintain single Zn atom in its respective roles in the photocatalytic NO oxidation. The distinctive Zn-O_2-NO structure produced a one-step route for NO oxidation, improving the fabrication of reactive oxygen species and converting NO directly to nitrate to avoid the secondary pollution of NO_2.

4. Conclusion

In conclusion, single Zn atom doped g-C_3N_4 (Zn-CN) with a high Zn amount of 37.0 wt% (10.2 at%) was fabricated through simple pyrolysis. Single Zn atoms were embedded between g-C_3N_4 layers to form the Zn-N_3 coordination structure. This fantastic Zn-N_3 structure improved visible light absorption and carrier separation efficiency. Moreover, a unique Zn-O_2-NO structure was formed after NO and O_2 co-adsorbed on Zn-CN surface, which turned the NO oxidation pathway to directly form nitrate and inhibit the fabrication of NO_2. This work demonstrates a promise single atom catalyst for purifying low-concentration contaminants in the environment.

Declaration of Competing Interest

The authors declare that they have no known competing financial interests or personal relationships that could have appeared to influence the work reported in this paper.

Data availability

Data will be made available on request.

Acknowledgements

We acknowledge the National key R&D project of China (2020YFA0710000), the Cheung Kong Scholars Programme of China, Sichuan Science and Technology Program (2020ZDZX0008, 2021ZYD0035, 2022YFH0084) and the technology innovation R&D project of Chengdu (2022-YF05-00978-SN). We thank the National Supercomputing Center in Shenzhen for the calculations support. We would like to thank the Institute for Beam Physics and Technology (IBPT) for the operation of the storage ring, the Karlsruhe Research Accelerator (KARA). We acknowledge the KIT light source for provision of instruments at the CAT-ACT beamline of the Institute of Catalysis Research and Technology (IKFT), in particular, Dr. Tim Prüßmann and Dr. Anna Zimina (IKFT) for their help and technical support during experiments.

References

[1] K. Duan, G. Sun, Y. Zhang, K. Yahya, K. Wang, J.M. Madden, P.V. Caldwell, E. C. Cohen, S.G. McNulty, Impact of air pollution induced climate change on water availability and ecosystem productivity in the conterminous United States, Clim. Change 140 (2017) 259–272.

[2] J. Ngarambe, S.J. Joen, C. Han, G.Y. Yun, Exploring the relationship between particulate matter, CO, SO2, NO2, O3 and urban heat island in Seoul, Korea. J. Hazard. Mater. 403 (2021), 123615.

[3] Y. Deng, X. Shi, L. Wei, H. Liu, J. Li, X. Ou, L. Dong, B. Li, Effect of intergrowth and coexistence CuO-CeO2 catalyst by grinding method application in the catalytic reduction of NOx by CO, J. Alloys Compd. 869 (2021), 159231.

[4] K. Zhao, X. Sun, C. Wang, X. Song, F. Wang, K. Li, P. Ning, Supported catalysts for simultaneous removal of SO2, NOx, and Hg0 from industrial exhaust gases: a review, Chin. Chem. Lett. 32 (10) (2021) 2963–2974.

[5] H. Wang, K. Li, J. Li, Y. Sun, F. Dong, Photochemical transformation pathways of nitrates from photocatalytic NOx oxidation: implications for controlling secondary pollutants, Environ. Sci. Technol. Lett. 8 (2021) 873–877.

[6] Y. Lu, Y. Huang, Y. Zhang, T. Huang, H. Li, J. Cao, W. Ho, Effects of H2O2 generation over visible light-responsive Bi/Bi2O2-xCO3 nanosheets on their photocatalytic NOx removal performance, Chem. Eng. J. 363 (2019) 374–382.

[7] H. Yu, W. Dai, G. Qian, X. Gong, D. Zhou, X. Li, X. Zhou, The NOx degradation performance of nano-TiO2 coating for asphalt pavement, Nanomaterials 10 (2020) 897.

[8] T. Maggos, A. Plassais, J. Bartzis, C. Vasilakos, N. Moussiopoulos, L. Bonafous, Photocatalytic degradation of NOx in a pilot street canyon configuration using TiO2-mortar panels, Environ. Monit. Assess. 136 (2008) 35–44.

[9] A. Giampiccolo, D.M. Tobaldi, S.G. Leonardi, B.J. Murdoch, M.P. Seabra, M. P. Ansell, G. Neri, R.J. Ball, Sol gel graphene/TiO2 nanoparticles for the photocatalytic-assisted sensing and abatement of NO2, Appl. Catal. B: Environ. 243 (2019) 183–194.

[10] P. Zhu, X. Yin, X. Gao, G. Dong, J. Xu, C. Wang, Enhanced photocatalytic NO removal and toxic NO2 production inhibition over ZIF-8-derived ZnO nanoparticles with controllable amount of oxygen vacancies, Chin. J. Catal. 42 (2021) 175–183.

[11] B. Qiao, A. Wang, X. Yang, L.F. Allard, Z. Jiang, Y. Cui, J. Liu, J. Li, T. Zhang, Single-atom catalysis of CO oxidation using Pt1/FeOx, Nat. Chem. 3 (2011) 634–641.

[12] A. Wang, J. Li, T. Zhang, Heterogeneous single-atom catalysis, Nat. Rev. Chem. 2 (2018) 65–81.

[13] H. Zhang, G. Liu, L. Shi, J. Ye, Single-atom catalysts: emerging multifunctional materials in heterogeneous catalysis, Adv. Energy Mater. 8 (2018) 1701343.

[14] Y. Chen, S. Ji, C. Chen, Q. Peng, D. Wang, Y. Li, Single-atom catalysts: synthetic strategies and electrochemical applications, Joule 2 (2018) 1242–1264.

[15] S.H. Talib, S. Hussain, S. Baskaran, Z. Lu, J. Li, Chromium single-atom catalyst with graphyne support: a theoretical study of NO oxidation and reduction, ACS Catal. 10 (2020) 11951–11961.

[16] W. Yang, X. Liu, X. Chen, Y. Cao, S. Cui, L. Jiao, C. Wu, C. Chen, D. Fu, I.D. Gates, Z. Gao, H. Jiang, A sulfur-tolerant MOF-based single-atom Fe catalyst for efficient oxidation of NO and Hg0, Adv. Mater. 34 (20) (2022) 2110123.

[17] Y. Tang, W. Chen, H. Zhang, Z. Wang, D. Teng, Y. Cui, Z. Feng, X. Dai, Single-atom metal-modified graphenylene as a high-activity catalyst for CO and NO oxidation, Phys. Chem. Chem. Phys. 22 (2020) 16224–16235.

[18] S. Chen, Y. Zhou, J. Li, Z. Hu, F. Dong, Y. Hu, H. Wang, L. Wang, K.K. Ostrikov, Z. Wu, Single-atom Ru-implanted metal–organic framework/MnO2 for the highly selective oxidation of NOx by plasma activation, ACS Catal. 10 (2020) 10185–10196.

[19] Y. Yao, Z. Huang, P. Xie, L. Wu, L. Ma, T. Li, Z. Pang, M. Jiao, Z. Liang, J. Gao, et al., High temperature shockwave stabilized single atoms, Nat. Nanotechnol. 14 (2019) 851–857.

[20] J. Guo, J. Huo, Y. Liu, W. Wu, Y. Wang, M. Wu, H. Liu, G. Wang, Nitrogen-doped porous carbon supported nonprecious metal single-atom electrocatalysts: from synthesis to application, Small Methods 3 (2019) 1900159.

[21] C.W. Bezerra, L. Zhang, K. Lee, H. Liu, A.L. Marques, E.P. Marques, H. Wang, J. Zhang, A review of Fe–N/C and Co–N/C catalysts for the oxygen reduction reaction, Electrochim. Acta 53 (2008) 4937–4951.

[22] W. Liu, L. Zhang, W. Yan, X. Liu, X. Yang, S. Miao, W. Wang, A. Wang, T. Zhang, Single-atom dispersed Co–N–C catalyst: structure identification and performance for hydrogenative coupling of nitroarenes, Chem. Sci. 7 (2016) 5758–5764.

[23] Y. Wang, X. Zhao, D. Cao, Y. Wang, Y. Zhu, Peroxymonosulfate enhanced visible light photocatalytic degradation bisphenol A by single-atom dispersed Ag mesoporous g-C3N4 hybrid, Appl. Catal. B: Environ. 211 (2017) 79–88.

[24] Z. Chen, J. Zhao, C.R. Cabrera, Z. Chen, Computational screening of efficient single-atom catalysts based on graphitic carbon nitride (g-C3N4) for nitrogen electroreduction, Small Methods 3 (2019) 1800368.

[25] S. An, G. Zhang, T. Wang, W. Zhang, K. Li, C. Song, J.T. Miller, S. Miao, J. Wang, X. Guo, High-density ultra-small clusters and single-atom Fe sites embedded in graphitic carbon nitride (g-C3N4) for highly efficient catalytic advanced oxidation processes, ACS Nano 12 (2018) 9441–9450.

[26] W. Ong, L. Tan, Y.H. Ng, S. Yong, S. Chai, Graphitic carbon nitride (g-C3N4)-based photocatalysts for artificial photosynthesis and environmental remediation: are we a step closer to achieving sustainability? Chem. Rev. 116 (2016) 7159–7329.

[27] J. Fu, J. Yu, C. Jiang, B. Cheng, g-C3N4-based heterostructured photocatalysts, Adv. Energy Mater. 8 (3) (2018) 1701503.

[28] R. Zhang, P. Li, F. Wang, L. Ye, A. Gaur, Z. Huang, Z. Zhao, Y. Bai, Y. Zhou, Atomically dispersed Mo atoms on amorphous g-C3N4 promotes visible-light absorption and charge carriers transfer, Appl. Catal. B: Environ. 250 (2019) 273–279.

[29] T. Xiong, W. Cen, Y. Zhang, F. Dong, Bridging the g-C3N4 interlayers for enhanced photocatalysis, ACS Catal. 6 (2016) 2462–2472.

[30] X. Wu, J. Cheng, X. Li, Y. Li, K. Lv, Enhanced visible photocatalytic oxidation of NO by repeated calcination of g-C3N4, Appl. Surf. Sci. 465 (2019) 1037–1046.

[31] J. Liao, W. Cui, J. Li, J. Sheng, H. Wang, X. Dong, P. Chen, G. Jiang, Z. Wang, F. Dong, Nitrogen defect structure and NO+ intermediate promoted photocatalytic NO removal on H2 treated g-C3N4, Chem. Eng. J. 379 (2020), 122282.

[32] K. Li, W. Cui, J. Li, Y. Sun, Y. Chu, G. Jiang, Y. Zhou, Y. Zhang, F. Dong, Tuning the reaction pathway of photocatalytic NO oxidation process to control the secondary pollution on monodisperse Au nanoparticles@g-C3N4, Chem. Eng. J. 378 (2019), 122184.

[33] M. Segall, P.J. Lindan, M. Probert, C.J. Pickard, P.J. Hasnip, S. Clark, M. Payne, First-principles simulation: ideas, illustrations and the CASTEP code, J. Phys.: Condens. Matter. 14 (2002) 2717.

[34] J.P. Perdew, K. Burke, M. Ernzerhof, Generalized gradient approximation made simple, Phys. Rev. Lett. 77 (1996) 3865.

[35] J. White, D. Bird, Implementation of gradient-corrected exchange-correlation potentials in Car-Parrinello total-energy calculations, Phys. Rev. B 50 (1994) 4954.

[36] R. Zhang, M. Ma, Q. Zhang, F. Dong, Y. Zhou, Multifunctional g-C3N4/graphene oxide wrapped sponge monoliths as highly efficient adsorbent and photocatalyst, Appl. Catal. B: Environ. 235 (2018) 17–25.

[37] W. Ong, L. Tan, S. Chai, S. Yong, A.R. Mohamed, Surface charge modification via protonation of graphitic carbon nitride (g-C3N4) for electrostatic self-assembly construction of 2D/2D reduced graphene oxide (rGO)/g-C3N4 nanostructures toward enhanced photocatalytic reduction of carbon dioxide to methane, Nano Energy 13 (2015) 757–770.

[38] R. Zhang, T. Ran, Y. Cao, L. Ye, F. Dong, Q. Zhang, L. Yuan, Y. Zhou, Oxygen activation of noble-metal-free g-C3N4/α-Ni(OH)2 to control the toxic byproduct of photocatalytic nitric oxide removal, Chem. Eng. J. 382 (2020), 123029.

[39] K. Katsumata, R. Motoyoshi, N. Matsushita, K. Okada, Preparation of graphitic carbon nitride (g-C3N4)/WO3 composites and enhanced visible-light-driven photodegradation of acetaldehyde gas, J. Hazard. Mater. 260 (2013) 475–482.

[40] G. Dong, D.L. Jacobs, L. Zang, C. Wang, Carbon vacancy regulated photoreduction of NO to N2 over ultrathin g-C3N4 nanosheets, Appl. Catal. B: Environ. 218 (2017) 515–524.

[41] Y. Cao, Q. Li, W. Wang, Construction of a crossed-layer-structure MoS2/g-C3N4 heterojunction with enhanced photocatalytic performance, RSC Adv. 7 (2017) 6131–6139.

[42] T. Kondo, S. Casolo, T. Suzuki, T. Shikano, M. Sakurai, Y. Harada, M. Saito, M. Oshima, M.I. Trioni, G.F. Tantardini, J. Nakamura, Atomic-scale characterization of nitrogen-doped graphite: effects of dopant nitrogen on the local electronic structure of the surrounding carbon atoms, Phys. Rev. B 86 (2012), 035436.

[43] C. Quir´os, J. G´omez-Garcıa, F. Palomares, L. Soriano, E. Elizalde, J. Sanz, Correlation between N 1s core level x-ray photoelectron and x-ray absorption spectra of amorphous carbon nitride films, Appl. Phys. Lett. 77 (2000) 803–805.

[44] M. Zhou, S. Wang, P. Yang, Z. Luo, R. Yuan, A.M. Asiri, M. Wakeel, X. Wang, Layered heterostructures of ultrathin polymeric carbon nitride and ZnIn2S4 nanosheets for photocatalytic CO2 reduction, Chem. Eur. J. 24 (2018) 18529–18534.

[45] D. Wang, Y. Hu, J. Zhao, L. Zeng, X. Tao, W. Chen, Holey reduced graphene oxide nanosheets for high performance room temperature gas sensing, J. Mater. Chem. A 2 (2014) 17415–17420.

[46] S.K. Das, C. Dickinson, F. Lafir, D.F. Brougham, E. Marsili, Synthesis, characterization and catalytic activity of gold nanoparticles biosynthesized with rhizopus oryzae protein extract, Green Chem. 14 (2012) 1322–1334.

[47] C. Kang, D. Kong, J. Yao, C. Guo, L. Wang, K. Xiao, C.F. Dong, Long-term monitoring of zinc corrosion behavior in typical hot and dry atmosphere environment in Turpan, China. Anti-Corros. Method. M. 65 (5) (2018) 471–483.

[48] M. Fang, X. Wang, X. Li, Y. Zhu, G. Xiao, J. Feng, X. Jiang, K. Lv, Y. Zhu, W.F. Lin, Curvature-induced Zn 3d electron return on Zn-N4 single-atom carbon nanofibers for boosting electroreduction of CO2, ChemCatChem 13 (2021) 603–609.

[49] L. Lin, T. Liu, J. Xiao, H. Li, P. Wei, D. Gao, B. Nan, R. Si, G. Wang, X. Bao, Enhancing CO2 electroreduction to methane with a cobalt phthalocyanine and zinc–nitrogen–carbon tandem catalyst, Angew. Chem. Int. Ed. 59 (2020) 22408–22413.

[50] P. Song, M. Luo, X. Liu, W. Xing, W. Xu, Z. Jiang, L. Gu, Zn single atom catalyst for highly efficient oxygen reduction reaction, Adv. Fun. Mater. 27 (2017) 1700802.

[51] C. Tang, Y. Jiao, B. Shi, J.N. Liu, Z. Xie, X. Chen, Q. Zhang, S.Z. Qiao, Coordination tunes selectivity: two-electron oxygen reduction on high-loading molybdenum single-atom catalysts, Angew. Chem. Int. Ed. 59 (2020) 9171–9176.

[52] J. Li, S. Chen, N. Yang, M. Deng, S. Ibraheem, J. Deng, J. Li, L. Li, Z. Wei, Ultrahigh-loading zinc single-atom catalyst for highly efficient oxygen reduction in both acidic and alkaline media, Angew. Chem. Int. Ed. 58 (2019) 7035–7039.

[53] J. Wang, Z. Li, Y. Wu, Y. Li, Fabrication of single-atom catalysts with precise structure and high metal loading, Adv. Mater. 30 (2018) 1801649.

[54] M.P. Ruggeri, I. Nova, E. Tronconi, J.A. Pihl, T.J. Toops, W.P. Partridge, In-situ DRIFTS measurements for the mechanistic study of NO oxidation over a commercial Cu-CHA catalyst, Appl. Catal. B: Environ. 166-167 (2015) 181–192.

[55] T. Baidya, P. Bera, B.D. Mukri, S.K. Parida, O. Kröcher, M. Elsener, M. Hegde, DRIFTS studies on CO and NO adsorption and NO+CO reaction over Pd2+- substituted CeO2 and Ce0.75Sn0.25O2 catalysts, J. Catal. 303 (2013) 117–129.

[56] H. Hu, S. Cai, H. Li, L. Huang, L. Shi, D. Zhang, In situ DRIFTs investigation of the low-temperature reaction mechanism over Mn-doped Co3O4 for the selective catalytic reduction of NOx with NH3, J. Phys. Chem. C 119 (2015) 22924–22933.

[57] M. Zhou, G. Dong, F. Yu, Y. Huang, The deep oxidation of NO was realized by Sr multi-site doped g-C3N4 via photocatalytic method, Appl. Catal. B: Environ. 256 (2019), 117825.
[58] J. Ma, C. Wang, H. He, Enhanced photocatalytic oxidation of NO over g-C3N4-TiO2 under UV and visible light, Appl. Catal. B: Environ. 184 (2016) 28–34.

[59] Z. Wang, Y. Huang, W. Ho, J. Cao, Z. Shen, S.C. Lee, Fabrication of Bi2O2CO3/g- C3N4 heterojunctions for efficiently photocatalytic NO in air removal: in-situ self-sacrificial synthesis, characterizations and mechanistic study, Appl. Catal. B: Environ. 199 (2016) 123–133.

[60] Y. Geng, D. Chen, N. Li, Q. Xu, H. Li, J. He, J. Lu, Z-Scheme 2D/2D α-Fe2O3/g-C3N4 heterojunction for photocatalytic oxidation of nitric oxide, Appl. Catal. B: Environ. 280 (2021), 119409.

[61] P. Chen, F. Dong, M. Ran, J. Li, Synergistic photo-thermal catalytic NO purification of MnOx/g-C3N4: enhanced performance and reaction mechanism, Chin. J. Catal. 39 (2018) 619–629.

[62] G. Dong, L. Yang, F. Wang, L. Zang, C. Wang, Removal of nitric oxide through visible light photocatalysis by g-C3N4 modified with perylene imides, ACS Catal. 6 (2016) 6511–6519.

[63] Q. Zheng, Y. Cao, N. Huang, R. Zhang, Y. Zhou, Selective exposure of BiOI oxygen-rich 110 facet induced by BN nanosheets for enhanced photocatalytic oxidation performance, Acta Phys.-Chim. Sin. 37 (2021) 2009063.

[64] I. Subbotina, D. Barsukov, Direct evidence of the key role of UV-formed peroxide species in photocatalytic gas–solid oxidation in air on anatase TiO2 particles, Phys. Chem. Chem. Phys. 22 (2020) 2200–2211.

[65] H. Kim, P.J. Rogler, S.K. Sharma, A.W. Schaefer, E.I. Solomon, K.D. Karlin, Heme-feIII superoxide, peroxide and hydroperoxide thermodynamic relationships: FeIII-O2·–complex H-atom abstraction reactivity, J Am. Chem. Soc. 142 (2020) 3104–3116.

[66] J. Shearer, R.C. Scarrow, J.A. Kovacs, Synthetic models for the cysteinate-ligated non-heme iron enzyme superoxide reductase: observation and structural characterization by XAS of an FeIII-OOH intermediate, J Am. Chem. Soc. 124 (2002) 11709–11717.

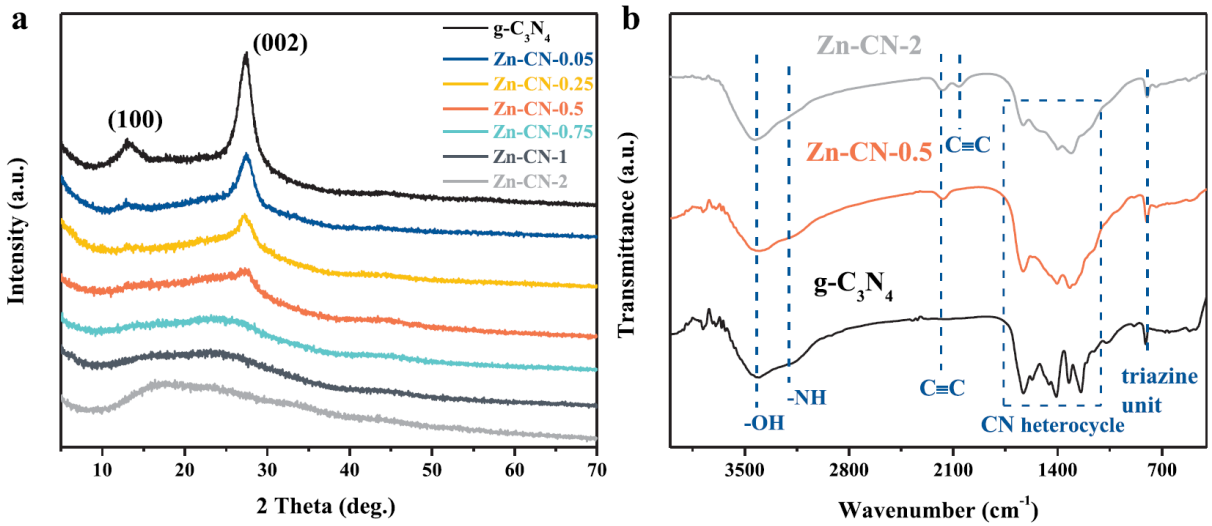

Figure 1. XRD patterns (a) and FTIR spectra (b) of different samples.

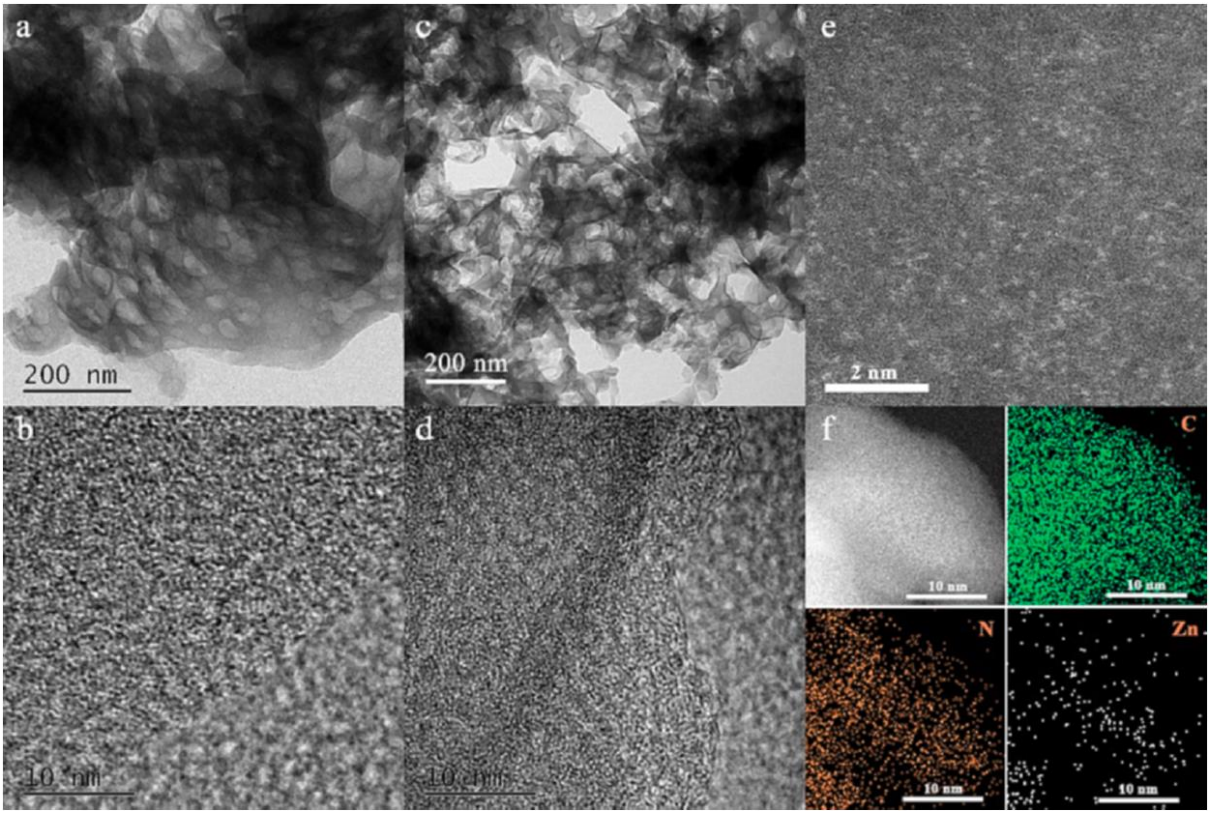

Figure 2. TEM and HRTEM images of g-C_3N_4 (a and b) and Zn-CN (c and d); HAADF-STEM image of Zn-CN (e) and corresponding EDS element mapping images (f).

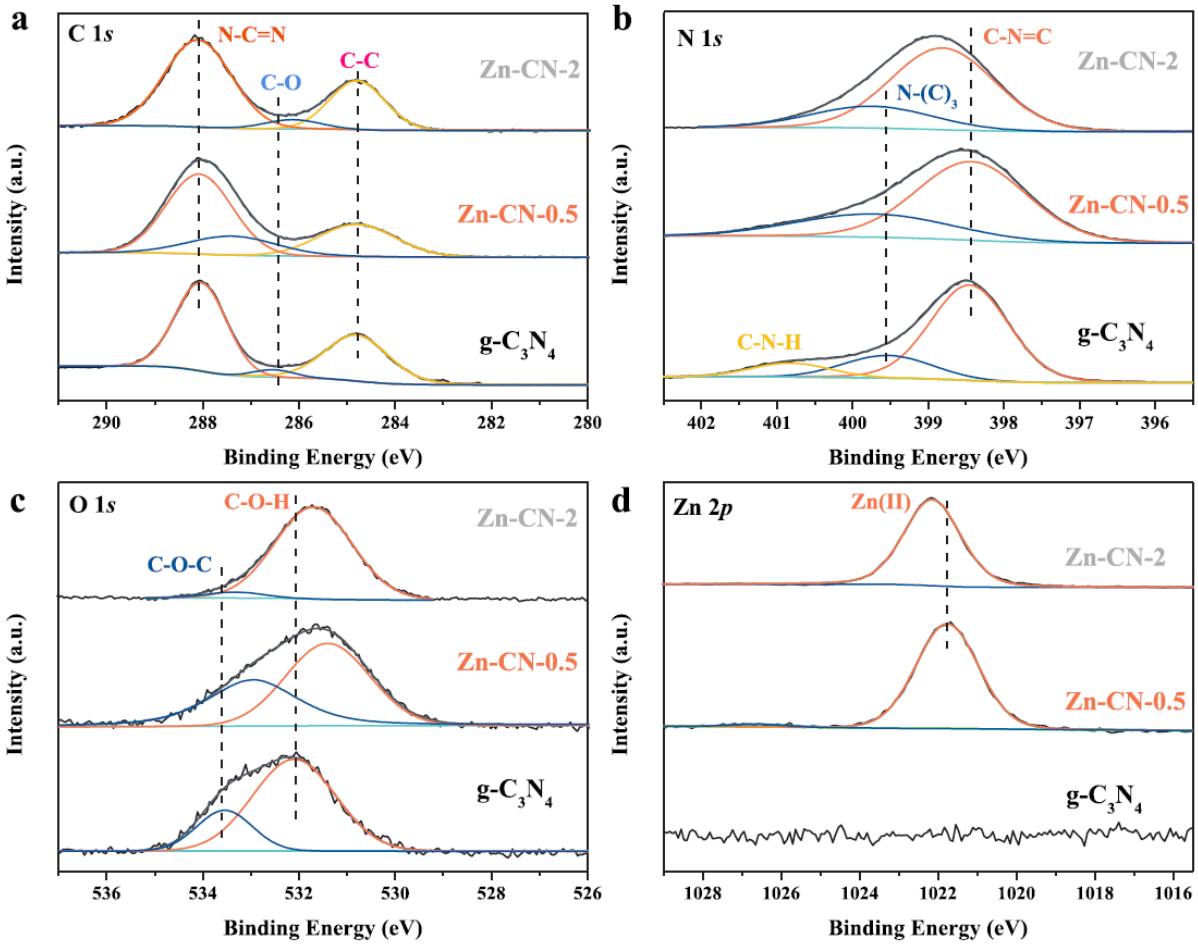

Figure 3. XPS of g-C3N4 and different ratio of Zn-CN: (a) C 1s; (b) N 1s; (c) O 1s; (d) Zn 2p.

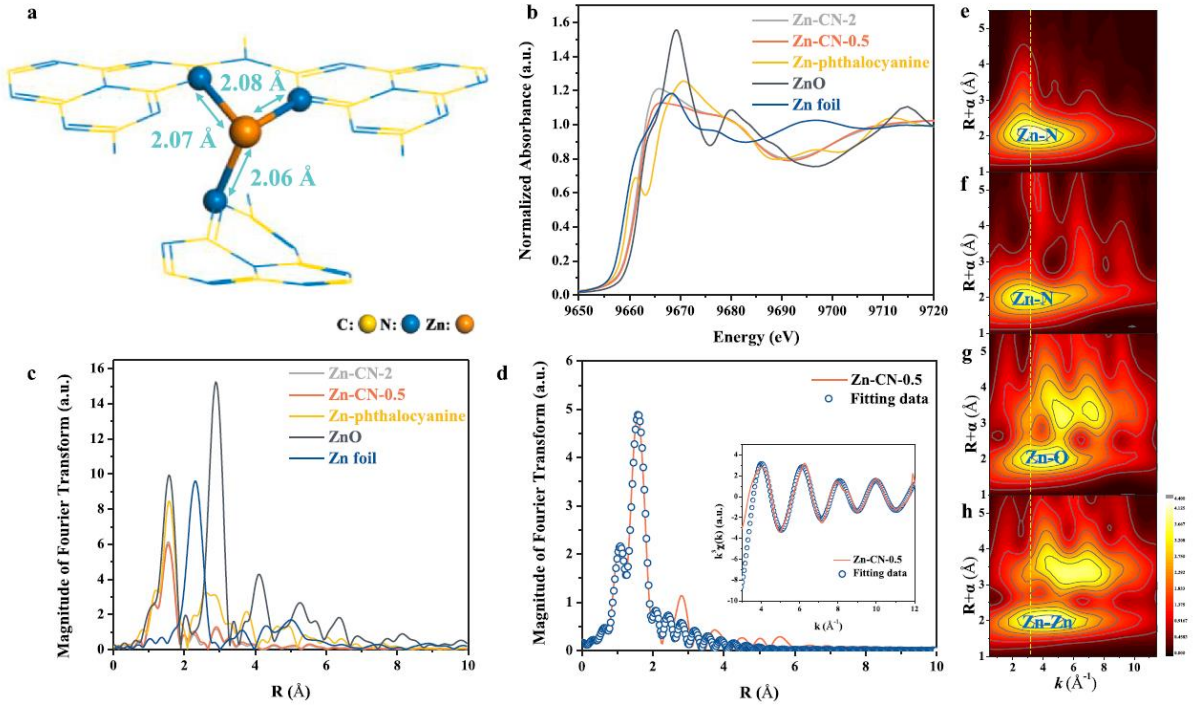

Figure 4. (a) DFT-calculated Zn-CN structure; XANES spectra (b) and EXAFS (c) of different samples; (d) EXAFS of Zn-CN-0.5 and its fitting data; the wavelet transform contour plots of Zn-CN (e), Zn phthalocyanine (f), ZnO (g) and Zn foil (h).

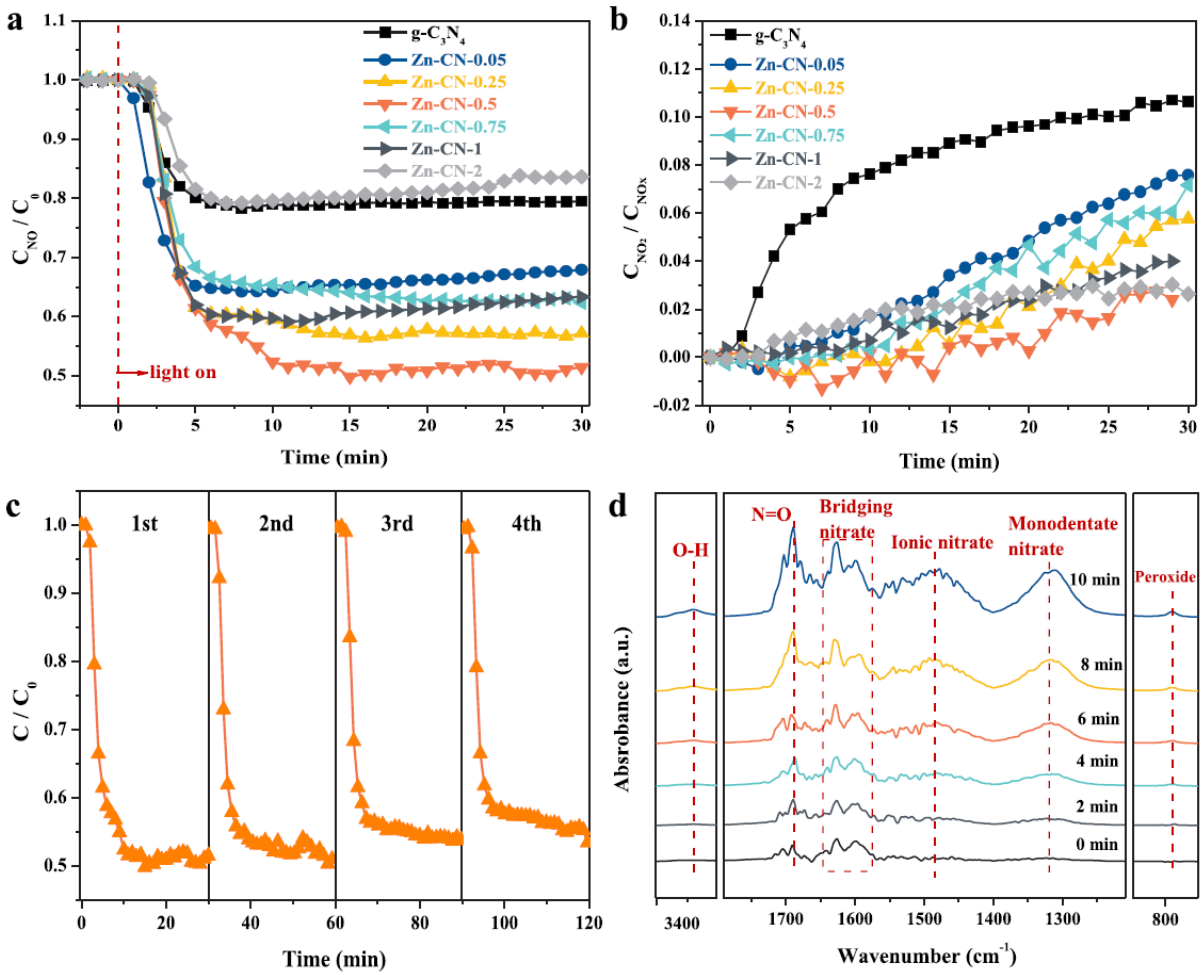

Figure 5. NO oxidation (a) and NO_2 fabrication (b) over different samples; (c) circle experiment of Zn-CN-0.5; (d) in situ DRIFTS of photocatalytic NO oxidation over Zn-CN-0.5.

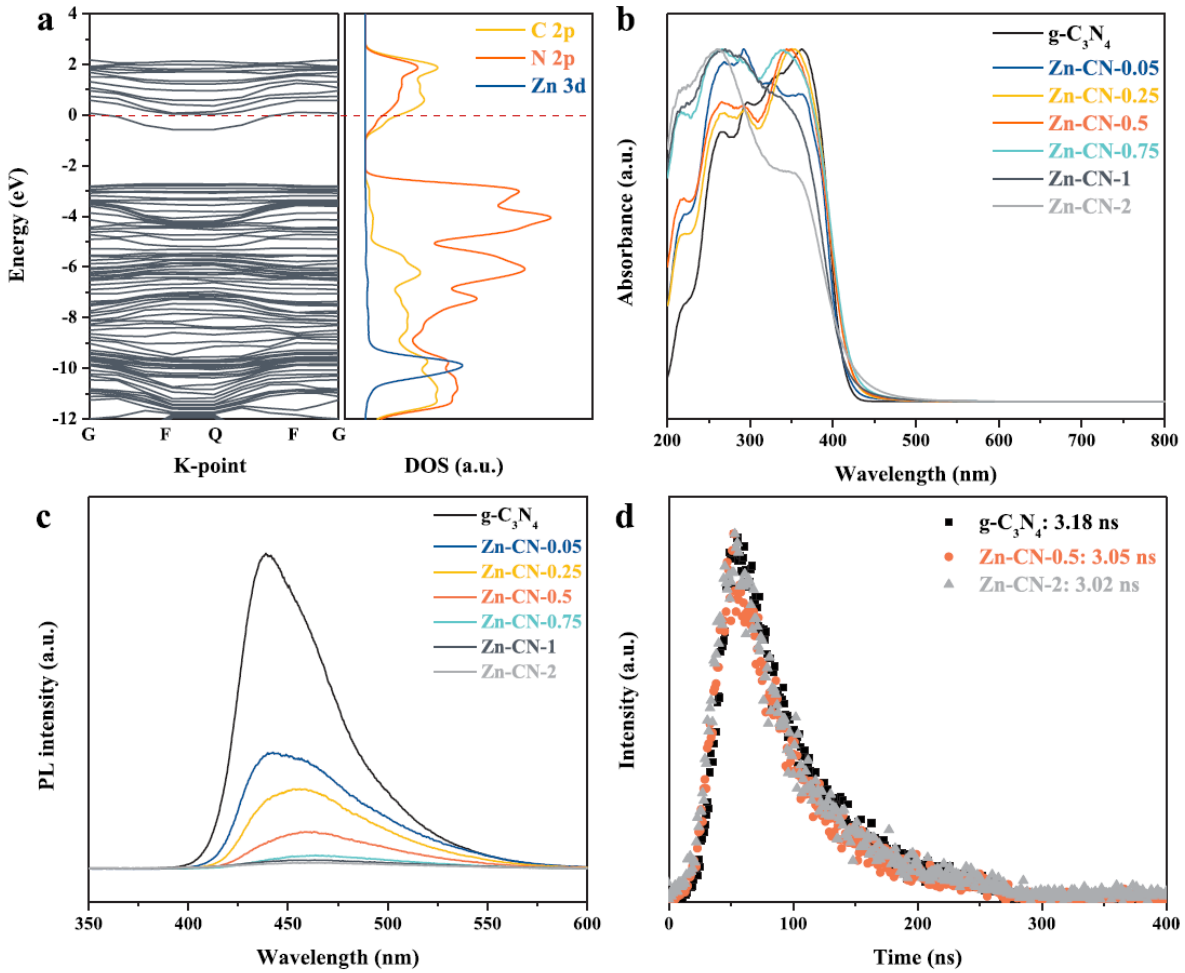

Figure 6. (a) Band structure and part density of state of Single Zn atom doped g-C_3N_4; UV–vis DRS (b), PL (c) and TRPL (d) of different samples.

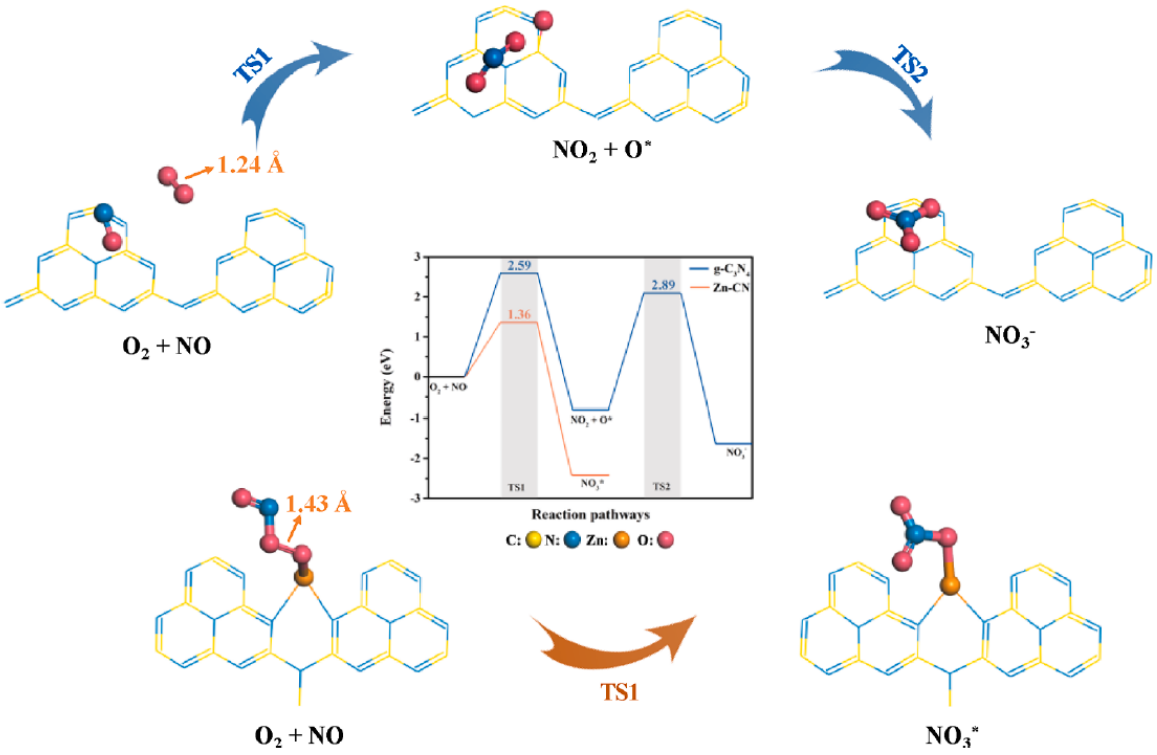

Figure 7. NO oxidation process over g-C_3N_4 and Zn-CN.

Supplementary Material

Single-atom dispersed Zn-N_3 active sites bridging the interlayer of g-C_3N_4 to tune NO oxidation pathway for the inhibition of toxic by-product generation

Ruiyang Zhang[a],[b], Yuehan Cao[b], Dmitry E. Doronkin[d], Minzhi Ma[b], Fan Dong[c], Ying Zhou*[a],[b]

[a] State Key Laboratory of Oil and Gas Reservoir Geology and Exploitation,

Southwest Petroleum University,

Chengdu, 610500, China

E-mail: yzhou@swpu.edu.cn

[b] Institute of Carbon Neutrality & School of New Energy and Materials,

Southwest Petroleum University,

Chengdu, 610500, China

[c] Research Center for Environmental and Energy Catalysis,

Institute of Fundamental and Frontier Sciences,

University of Electronic Science and Technology of China,

Chengdu 611731, China

[d] Institute of Catalysis Research and Technology and Institute for Chemical Technology and polymer chemistry,

Karlsruhe Institute of Technology,

Karlsruhe, 76131, Germany

Content

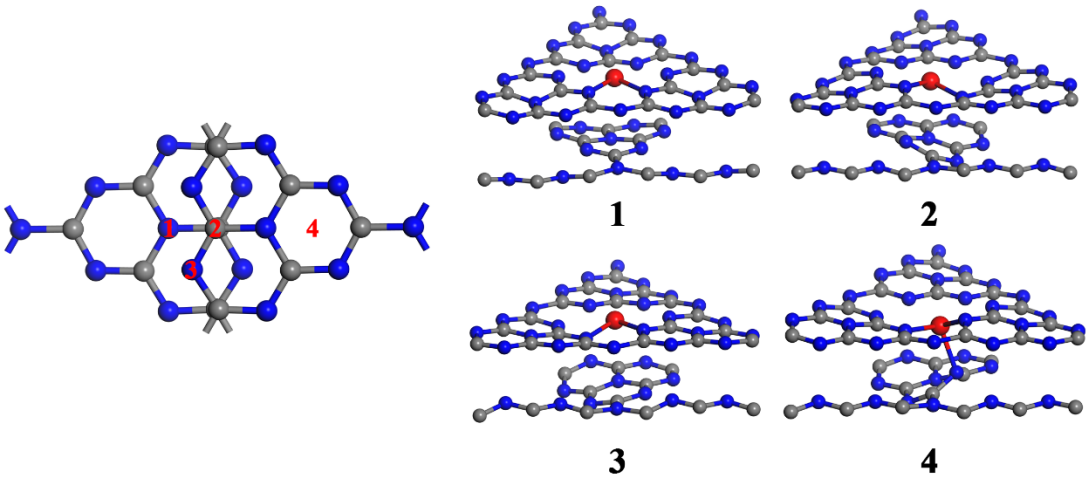

Figure S1 The points that single Zn atom intercalates into the layers of g-C_3N_4 and the DFT-optimized structures.

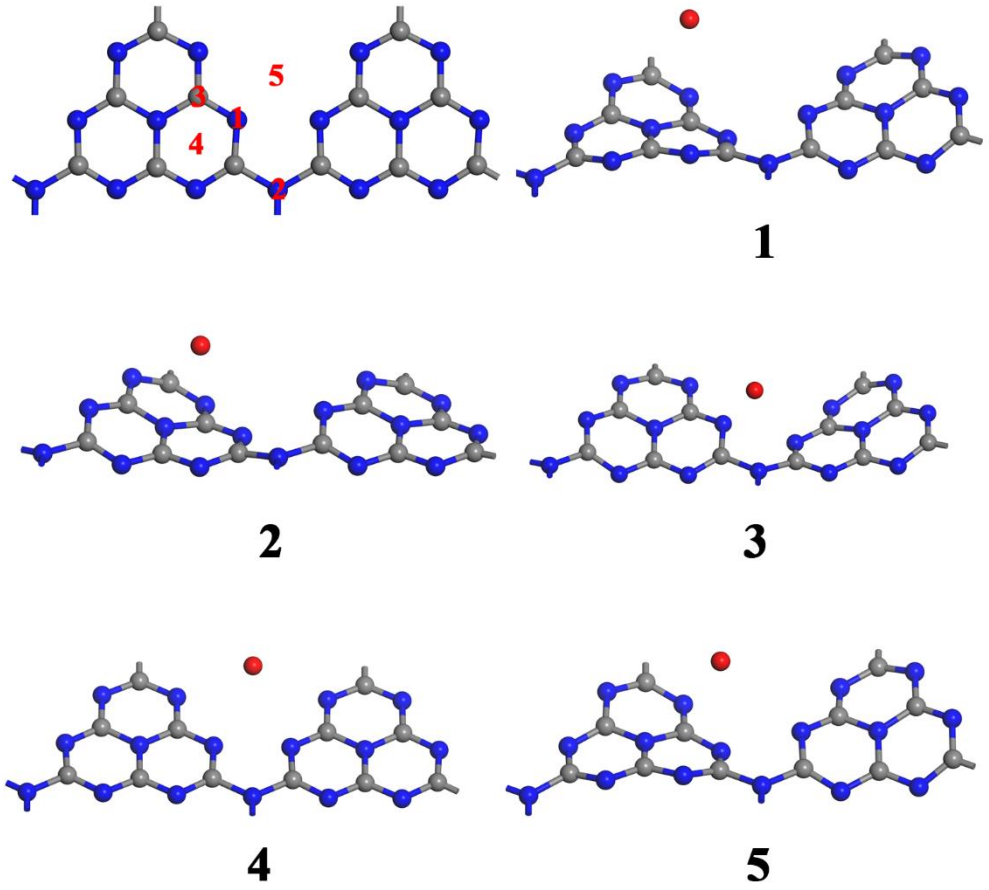

Figure S2 The points that single Zn atom loads on the surface of g-C_3N_4 and the DFT-optimized structures.

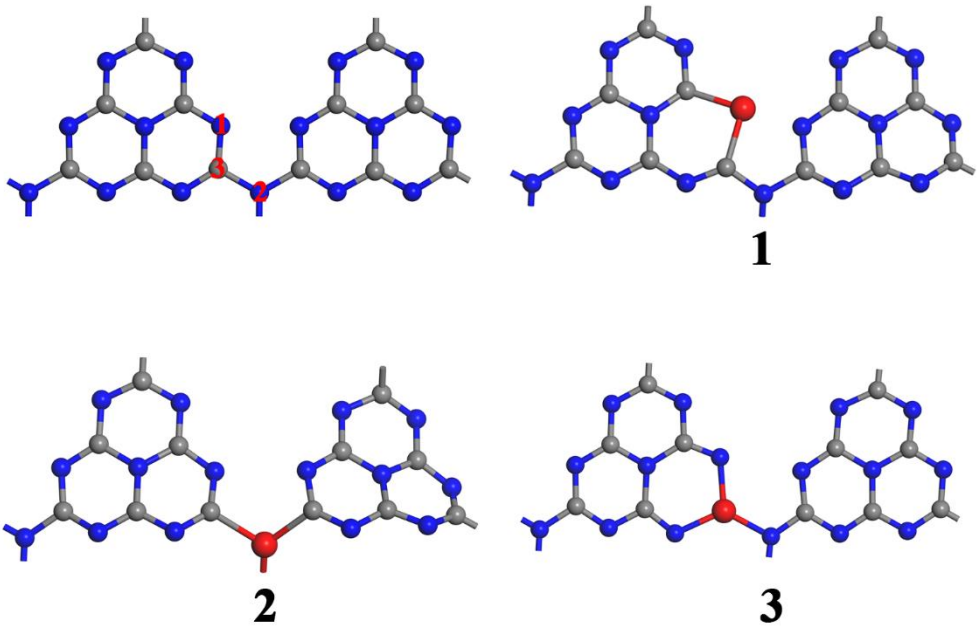

Figure S3 The points that single Zn atom replaces the N or C atom of g-C_3N_4 and the DFT-optimized structures.

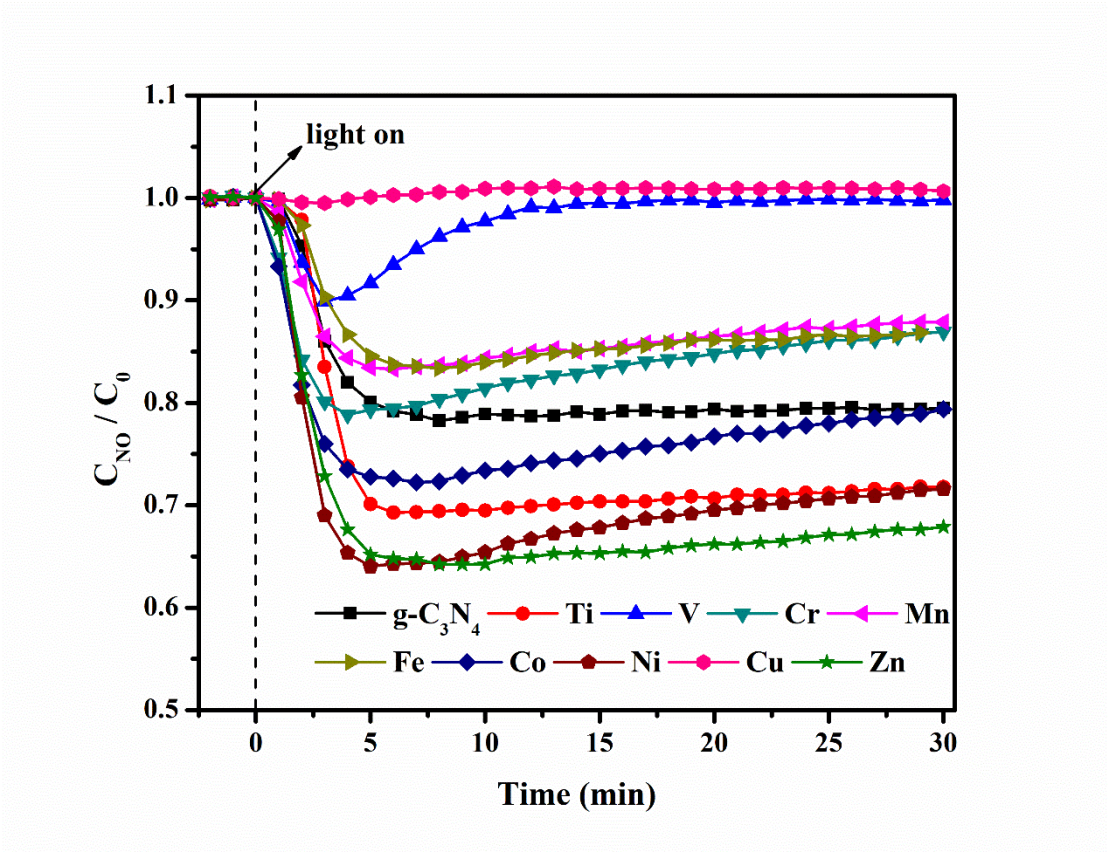

Figure S4 Photocatalytic NO oxidation over different transition metal-doped g-C_3N_4.

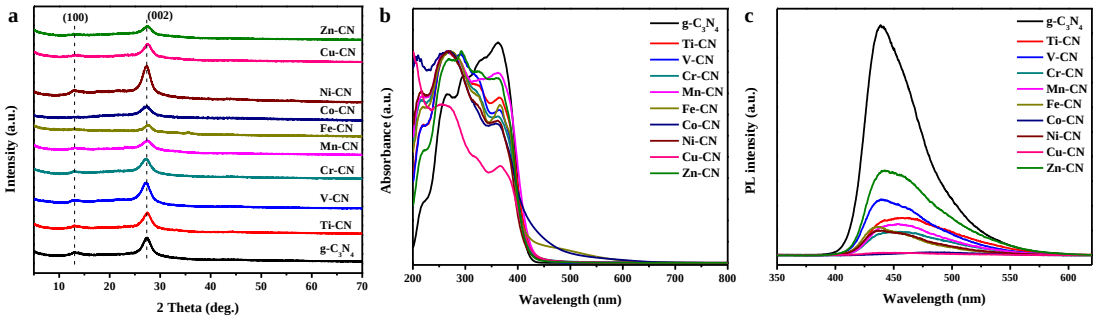

Figure S5 XRD patterns (a), UV-vis (b) and PL (c) spectra of different metal-doped g-C_3N_4.

Fig. S5a displays the XRD patterns of different metal-doped g-C_3N_4 materials. The two diffraction peaks in all of the samples are assigned to the g-C_3N_4 (100) and (002) planes, and there are no peaks for metal compounds, which may be because the metal compounds are amorphous or highly dispersed. In addition, the addition of the V and Ni atoms improves the crystallinity of g-C_3N_4 while others reduce that. It should be observed that with the addition of the metal atoms, the peak location of the (002) plane varies with various levels, revealing the altered structure of g-C_3N_4. The preceding data, however, cannot prove that Zn-Cn and other samples vary significantly from one another, nor can it be said with certainty that other metal-doped materials do not also produce single-atom catalysts, which need more elaborate characterizations.

The light adsorption of different samples is displayed in Fig. S5b. It is evident that the addition of metal atoms significantly affects the light absorption of g-C_3N_4. After doping with Ti, V, Cr, Mn, Co, Cu, and Zn, the band gap is decreased to 2.81, 2.99, 2.97, 2.92, 2.70, 2.91, and 2.99 eV, whereas it rises to 3.02 eV after doping with Fe and remains unchanged after doping with Ni. Zn-CN does not, however, exhibit the highest ability for light absorption, which may not be the determining factor for enhanced photocatalytic activity.

The PL spectra of different samples are shown in Fig. S5c. All samples exhibit decreased PL intensity with the addition of metal atoms because the Schottky barrier between the metal and g-C_3N_4 is formed, facilitating the transfer of electrons and preventing the recombination of electron-hole pairs. Additionally, when compared to other metal-doped g-C_3N_4 samples, Zn-CN exhibits the

greatest PL intensity, which may be due to its abundant defect structure. The defect locations are known to be active and frequently take part in the reaction as active centers. So, based on our best guess, more active sites rise with Zn doping, promoting photocatalytic NO oxidation.

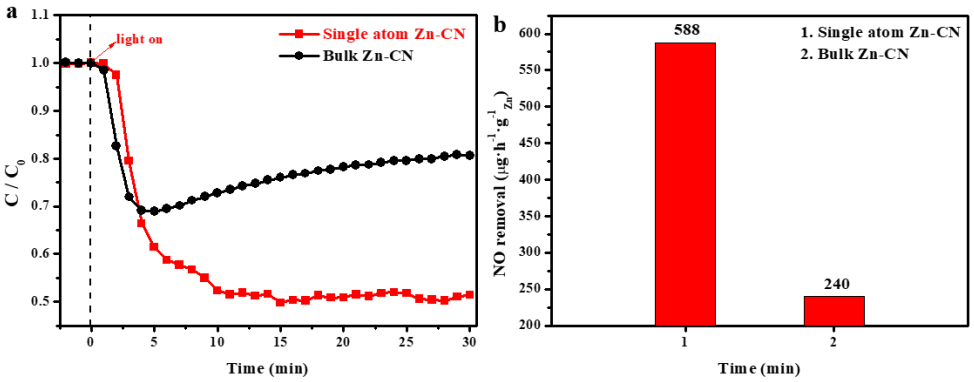

Figure S6 NO oxidation over single atom Zn-CN and bulk Zn-CN.

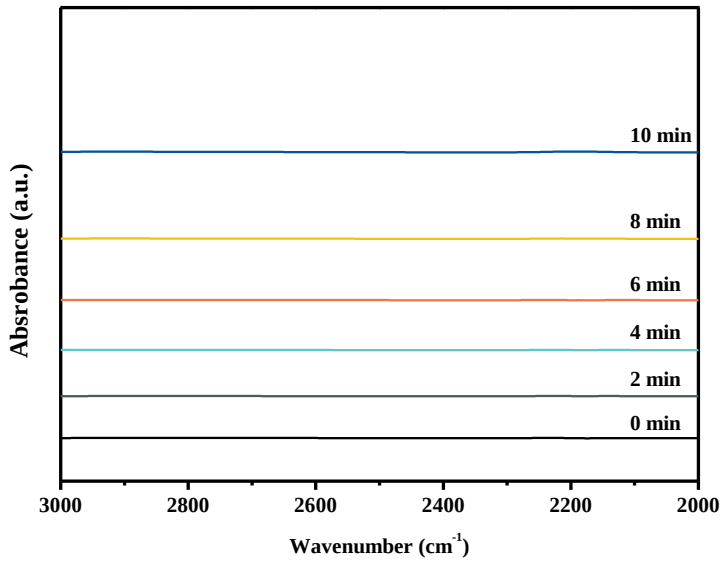

Figure S7 in situ DRIFTS of photocatalytic NO oxidation over Zn-CN-0.5.

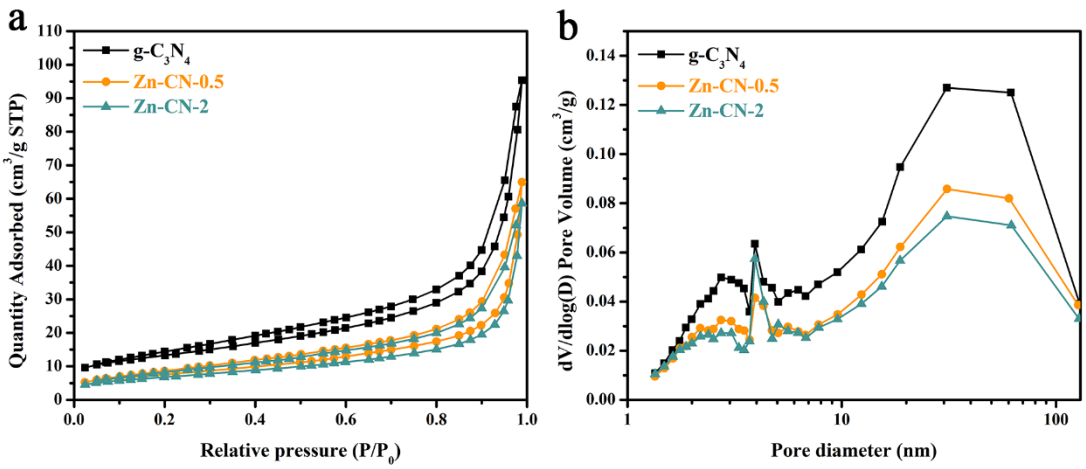

Figure S8 N_2 adsorption and desorption isotherms and BJH pore diameter distribution of Zn-CN compared with g-C_3N_4.

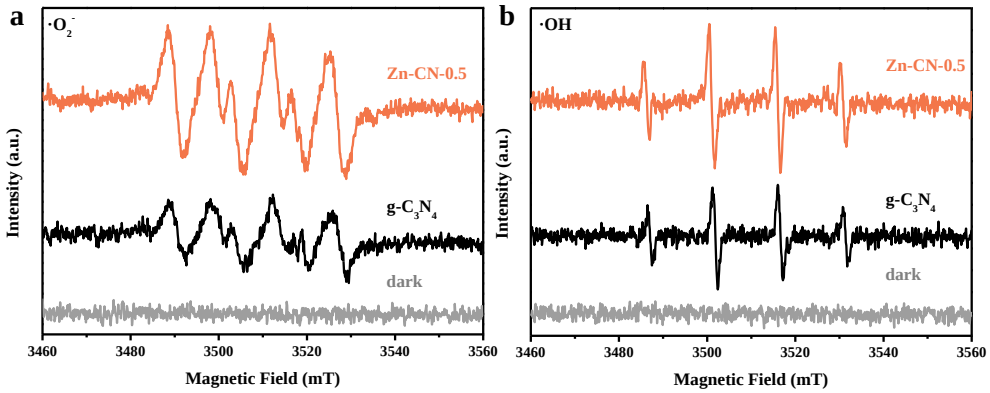

Figure S9 ESR spectra of g-C_3N_4 and Zn-CN-0.5.

Table S1. Formation energy and average bond length

	Point	Formation energy (eV)	Average bond length (Å)
Intercalation	1	-0.92	2.14
	2	-0.60	2.14
	3	-1.03	2.12
	4	-1.14	2.07
Load	1	-1.04	3.91
	2	-0.83	3.49
	3	-1.06	3.80
	4	-0.77	3.30
	5	-0.07	2.37
Replace	1	0.62	1.97
	2	2.07	1.76
	3	2.28	1.93

Table S2 Structural parameters obtained from the EXAFS fitting

Sample	Bond	CN	R (Å)	σ^2 × 10^{-3} (Å^2)	ΔE_0 (eV)	R-factor (%)
Zn-CN-0.5	Zn-N	3#	2.007 ± 0.005	7.6 ± 1	2.00#	2

CN: coordination number; R: Zn-N bond distance; σ^2: Debye-Waller factor; ΔE_0: Inner potential correction; R-factor: the goodness of the fit.

#：fixed value

Table S3 Comparison of the performance of different photocatalysts in NO oxidation

Catalyst	Conditions	NO removal (%)	NO_2 production (%)	Ref.
g-C_3N_4	Catalyst: 0.2 g; LED lamp: λ > 400 nm; NO: 600 ppb	35.8%	11.7%	30
N defects g-C_3N_4	Catalyst: 0.1 g; halogen tungsten lamp: 150 W, λ > 420 nm; NO: 600 ppb	41.8%	30%	31
Au/g-C_3N_4	Catalyst: 0.2 g; halogen tungsten lamp: 150 W, λ > 420 nm; NO: 500 ppb	41.0%	< 10%	32
Sr/g-C_3N_4	Catalyst: 0.05 g; Xe lamp: 300 W, λ > 420 nm; NO: 600 ppb	55.0%	12.7%	57
g-C_3N_4-TiO_2	Catalyst: 0.05 g; Xe lamp: 500 W, λ > 420 nm; NO: 400 ppb	44.0%	36%	58
$Bi_2O_2CO_3$/g-C_3N_4	Catalyst: 0.1 g Xe lamp: 300 W, λ > 420 nm; NO: 400 ppb	34.8%	9.25%	59
α-Fe_2O_3/g-C_3N_4	Catalyst: 0.1 g; Xe lamp: 300 W, λ > 400 nm; NO: 600 ppb	60.8%	-	60
MnO_x/g-C_3N_4	Catalyst: 0.1 g; halogen tungsten lamp: 150 W, λ > 400 nm; NO: 500 ppb	44%	-	61
PI-g-C_3N_4	Catalyst: 0.05 g; Xe lamp: 300 W, λ > 420 nm; NO: 600 ppb	47%	1.7%	62
Zn-CN	Catalyst: 0.1 g; Xe lamp: 150 W, λ > 420 nm; NO: 600 ppb	49%	2.6%	This work

Table S4 Surface area and pore size

Sample	Surface area (m^2/g)	Pore volume (cc/g)	Average pore diameter (nm)
g-C_3N_4	46.3	0.14	12.7
Zn-CN-0.5	26.9	0.10	14.9
Zn-CN-2	24.3	0.09	14.9